Surv Geophys (2017) 38:479–502
DOI 10.1007/s10712-016-9395-x

Gravity Anomalies of Arbitrary 3D Polyhedral Bodies with Horizontal and Vertical Mass Contrasts

Zhengyong Ren[1,2] · Chaojian Chen[1,2] · Kejia Pan[3] · Thomas Kalscheuer[4] · Hansruedi Maurer[5] · Jingtian Tang[1,2]

Received: 28 July 2016 / Accepted: 24 October 2016 / Published online: 21 November 2016

Abstract During the last 15 years, more attention has been paid to derive analytic formulae for the gravitational potential and field of polyhedral mass bodies with complicated polynomial density contrasts, because such formulae can be more suitable to approximate the true mass density variations of the earth (e.g., sedimentary basins and bedrock topography) than methods that use finer volume discretization and constant density contrasts. In this study, we derive analytic formulae for gravity anomalies of arbitrary polyhedral bodies with complicated polynomial density contrasts in 3D space. The anomalous mass density is allowed to vary in both horizontal and vertical directions in a polynomial form of $\lambda = ax^m + by^n + cz^t$, where m, n, t are nonnegative integers and a, b, c are coefficients of mass density. First, the singular volume integrals of the gravity anomalies are transformed to regular or weakly singular surface integrals over each polygon of the polyhedral body. Then, in terms of the derived singularity-free analytic formulae of these surface integrals, singularity-free analytic formulae for gravity anomalies of arbitrary polyhedral bodies with horizontal and vertical polynomial density contrasts are obtained. For an arbitrary polyhedron, we successfully derived analytic formulae of the gravity potential and the gravity field in the case of $m \leq 1$, $n \leq 1$, $t \leq 1$, and an analytic formula of the gravity potential in the case of $m = n = t = 2$. For a rectangular prism, we derive an analytic formula of the gravity potential for $m \leq 3$, $n \leq 3$ and $t \leq 3$ and closed forms of the gravity field are presented for $m \leq 1$, $n \leq 1$ and $t \leq 4$. Besides generalizing previously published closed-form solutions for cases of constant and linear mass density contrasts to

✉ Kejia Pan
pankejia@hotmail.com

[1] Key Laboratory of Metallogenic Prediction of Nonferrous Metals and Geological Environment Monitoring, Ministry of Education (Central South University), Changsha 410083, Hunan, China

[2] School of Geosciences and Info-Physics, Central South University, Changsha 410083, Hunan, China

[3] School of Mathematics and Statistics, Central South University, Changsha 410083, Hunan, China

[4] Department of Earth Sciences, Uppsala University, 75236 Uppsala, Sweden

[5] Department of Earth Sciences, Institute of Geophysics, ETH Zurich, 8092 Zurich, Switzerland

higher polynomial order, to our best knowledge, this is the first time that closed-form solutions are presented for the gravitational potential of a general polyhedral body with quadratic density contrast in all spatial directions and for the vertical gravitational field of a prismatic body with quartic density contrast along the vertical direction. To verify our new analytic formulae, a prismatic model with depth-dependent polynomial density contrast and a polyhedral body in the form of a triangular prism with constant contrast are tested. Excellent agreements between results of published analytic formulae and our results are achieved. Our new analytic formulae are useful tools to compute gravity anomalies of complicated mass density contrasts in the earth, when the observation sites are close to the surface or within mass bodies.

Keywords Gravity · Singularity-free · Polyhedral body · Prism · Horizontal and vertical mass contrasts

1 Introduction

Gravitational data sets, which are measured using gravimeters based on land, in boreholes or on board satellites, aircraft or marine vessels, are used to estimate locations and shapes of embedded anomalous mass density bodies in the earth. For instance, gravity signal extraction and enhancement techniques (Zhang et al. 2014) can be used to estimate the approximated shapes of anomalous mass bodies in the underground. To more accurately determine depths, volumes and densities of anomalies, elaborate gravity inversion algorithms are employed (Li and Oldenburg 1998). To obtain more comprehensive and less ambiguous models of the earth, gravity data have been jointly inverted with other geophysical data sets, such as seismic data and electromagnetic induction data using constraints that couple the models of the different material parameters structurally or petrophysically (Moorkamp et al. 2011; Roberts et al. 2016). In recent years, rapid improvement in gravimeter efficiency and modern inversion algorithms has enhanced the capability of collecting large gravity data sets over large-scale areas and inverting such data sets for 3D density models (Kamm et al. 2015). These two improvements guarantee the wide application of the gravity methods in different geophysical or geodetic problems, such as mineral exploration (Beiki and Pedersen 2010; Lelièvre et al. 2012; Martinez et al. 2013; Kamm et al. 2015; Abtahi et al. 2016), crustal structure and Moho studies (Van der Meijde et al. 2013; De Castro et al. 2014) and geoid determination (Bajracharya and Sideris 2004).

An accurate gravity modeling solver plays a key role in interpreting or inverting gravity data sets. Generally, the structure of the real earth has complicated geometrical shapes and mass density distributions. Thus, the important question arises of how to efficiently approximate the 3D mass structure of the earth by volume discretization techniques. As an arbitrary mass body can be reasonably well represented by a set of disjoint polyhedral bodies with simple mass distributions, an arbitrary polyhedral body is generally adopted to reduce to maximum extend geometrical discretization errors. Therefore, seeking an accurate gravity modeling solver using 3D polyhedra is an essential step. Currently, different approaches can be adopted to evaluate the gravity anomaly caused by a polyhedral mass body, such as finite element methods (Kaftan et al. 2005; Cai and Cy 2005), finite difference methods (Farquharson and Mosher 2009), finite volume methods (Jahandari and

Farquharson 2013) and direct Newton integral methods (Blakely 1996). The finite element, finite difference and the finite volume methods translate the Poisson boundary value problem of the gravity potential into a system of linear equations. Then, linear system solvers are used to obtain the gravity potential. However, the accuracies of the gravity anomalies calculated by these three algorithms do not only depend on the quality of the discretization elements and the accuracies of the solvers for systems of linear equations, but also depend on the accuracies of the numerical techniques to translate the computed gravitational potentials into gravity fields. Therefore, in general, numerical solutions provided by these solvers are less accurate than solutions from direct Newton integral methods. As for the direct Newton integral methods, if we can derive analytic formulae of the gravity anomaly for a polyhedral mass body, the highest accuracies can be achieved. Therefore, to find possible analytic formulae has become an essential topic in gravity modeling problems using direct Newton integral approaches.

When the distance from the observation site to the mass body is much larger than the size of the polyhedral body, a constant mass density can be assigned to each polyhedral body in gravity forward modeling and inversion. Aiming to improve accuracy and efficiency, different analytic formulae were derived for a homogeneous (with constant mass density contrast) polyhedral body (Paul 1974; Barnett 1976; Okabe 1979; Pohanka 1988; Werner 1994; Holstein and Ketteridge 1996; Petrović 1996; Tsoulis and Petrović 2001; Holstein 2002; D'Urso 2013, 2014a; Conway 2015), for a homogeneous prismatic polyhedron (Nagy 1966; Banerjee and Das Gupta 1977; Smith 2000; Nagy et al. 2000; Tsoulis et al. 2003) and for a circular disk or a flat lamina (Conway 2016) during the last four decades.

Seeking simplicity, researchers generally assumed that the earth is composed of 3D anomalies in a layered medium or a succession of strata with horizontally undulating interfaces (e.g., sedimentary basins and underlying bedrock). In each layer, the rock mass density predominantly exhibits depth-dependent variations (García-Abdeslem 1992). Different efforts were made to derive analytic formulae for anomalous masses with internal layering such as exponential depth-dependent mass density variations (Chai and Hinze 1988), quadratic polynomial depth-dependent mass density variations (Rao 1990) and cubic polynomial depth-dependent mass density variations (García-Abdeslem 2005).

However, geological formations can be more complicated so that the above assumption of dominant depth-dependent mass density variations can be inappropriate. Also, exogenetic (e.g., weathering, fluvial, coastal and glacial) and endogenetic processes (e.g., diagenesis of rocks, plate tectonics, volcano eruptions and earthquakes) at different scales generally have changed the mass density structures of crust and mantle into 3D structures with both horizontal and vertical variations in mass density (Martín-Atienza and García-Abdeslem 1999). Therefore, it is critical for us to establish more general density distribution models for the mass bodies in the earth. This leads to the necessity of developing formulae capable of computing gravity responses of a polyhedral body with both horizontal and vertical variations in mass density (Zhou 2009b). Until now, only a few studies have been carried out on this more and more important topic. For instance, for a 3D polyhedral body with linear mass density varying in both horizontal and vertical directions, several authors derived different closed-form solutions by using different techniques (Pohanka 1998; Hansen 1999; Holstein 2003; Hamayun and Tenzer 2009; D'Urso 2014b). For a 3D prismatic body with arbitrary density contrast variations in both horizontal and vertical directions, Zhou (2009a) derived a generalized numerical solution in terms of 1D line integrals for the gravity anomaly. However, singularities exist in these 1D line integrals when the observation point is placed on any of the faces of the rectangular prism or

inside the prism. Therefore, more careful treatment should be considered to deal with singularities. More recently, for a 2D polygon body with polynomial density contrast variations in both horizontal and vertical directions, D'Urso (2015) derived singularity-free closed-form solutions using the generalized Gauss theorem, in which the mass density polynomials have up to cubic order.

However, to our best knowledge, there are still no publications that deal with analytic formulae for 3D polyhedral bodies with complicated polynomial mass density variations in both horizontal and vertical directions. In this study, we derive closed-form solutions for a 3D polyhedral body (and a prismatic body as a specific example) with mass density contrast as $\lambda = ax^m + by^n + cz^t$, where m, n, t are nonnegative integers and a, b, c are coefficients of mass density. Using several simple vector identities and integration by parts, we first transform the volume integrals of the gravity anomalies into a set of surface integrals over each polygon of the polyhedral body. Then, singularity-free analytic formulae are derived for these surface integrals. Finally, we obtain a set of completely singularity-free analytic formulae of gravity anomalies for arbitrary polyhedral bodies with horizontal and vertical polynomial density contrasts. Our analytic formulae are the first to (1) generalize previously published closed-form solutions for cases of constant mass density contrasts (Paul 1974; Barnett 1976; Okabe 1979; Pohanka 1988; Werner 1994; Holstein and Ketteridge 1996; Petrović 1996; Tsoulis and Petrović 2001; D'Urso 2013, 2014a; Conway 2015) and linear mass density contrasts (Pohanka 1998; Hansen 1999; Holstein 2003; Hamayun and Tenzer 2009; D'Urso 2014b, 2016) to higher polynomial order, (2) permit computation of the gravitational potential for a general polyhedral body with quadratic density contrast in all spatial directions using closed-form solutions and (3) permit computation of the vertical gravitational field for a prismatic body with quartic density contrast along the vertical direction using closed-form solutions. Additionally, our analytic formulae are singularity-free, which means the observation site can be located anywhere with respect to the mass body. Consequently, our singularity-free analytic formulae can be used in gravity modeling problems with high accuracy requirements such as terrain correction problems (where the observation sites locate on the earth's surface) and borehole gravity problems (where the observation sites are very close to the mass targets).

To verify our new analytic formula, a prismatic body with different depth-dependent polynomial variations and a polyhedral body in form of a triangular prism with constant density contrasts are examined. Excellent agreement between the published solutions (Blakely 1996; García-Abdeslem 2005; Tsoulis 2012) and our solutions is obtained.

2 Theory

2.1 Reduction of Order of Singularities

Given a polyhedral body H, a local Cartesian coordinate system is built in a way where the observation site $\mathbf{r}'$ is coincident with the coordinate origin, that is, $\mathbf{r}' = (0, 0, 0)$. Then, the polynomial mass density contrast in body H can be defined as:

$$\lambda(\mathbf{r}) = ax^m + by^n + cz^t, \tag{1}$$

where $\mathbf{r} = (x, y, z)$ is a source point. The coefficients a, b, c, m, n, t are generally estimated by fitting the gravity responses generated by the mass density function $\lambda(\mathbf{r})$ to the gravity data set collected in the field (Grant and West 1965). The integer values m, n, t are

the polynomial orders of the mass density. Then, the gravity potential and the gravity field are expressed as:

$$\phi(\mathbf{r}') = G \iiint_H \frac{\lambda(\mathbf{r})}{R} \mathrm{d}v, \tag{2}$$

$$\mathbf{g}(\mathbf{r}') = \nabla_{\mathbf{r}'} \phi(\mathbf{r}') = -G \iiint_H \lambda(\mathbf{r}) \nabla_{\mathbf{r}} \left(\frac{1}{R}\right) \mathrm{d}v, \tag{3}$$

where $R = |\mathbf{r} - \mathbf{r}'|$ and $G = 6.673 \times 10^{-11}\,\mathrm{m}^3\,\mathrm{kg}^{-1}\,\mathrm{s}^{-2}$ is the gravitational attraction constant.

2.1.1 Gravitational Potential

Substituting the polynomial mass contrast in Eq. (1) into Eqs. (2) and (3), we have

$$\begin{aligned} \phi(\mathbf{r}')_{mnt} &= aG \iiint_H \frac{x^m}{R} \mathrm{d}v + bG \iiint_H \frac{y^n}{R} \mathrm{d}v + cG \iiint_H \frac{z^t}{R} \mathrm{d}v \\ &= aG\phi_m^x + bG\phi_n^y + cG\phi_t^z, \end{aligned} \tag{4}$$

$$\begin{aligned} \mathbf{g}(\mathbf{r}')_{mnt} &= -aG \iiint_H x^m \nabla_{\mathbf{r}} \left(\frac{1}{R}\right) \mathrm{d}v - bG \iiint_H y^n \nabla_{\mathbf{r}} \left(\frac{1}{R}\right) \mathrm{d}v - cG \iiint_H z^t \nabla_{\mathbf{r}} \left(\frac{1}{R}\right) \mathrm{d}v \\ &= -aG\mathbf{g}_m^x - bG\mathbf{g}_n^y - cG\mathbf{g}_t^z, \end{aligned} \tag{5}$$

where ϕ_m^x, ϕ_n^y and ϕ_t^z denote the gravity potential contributed from mass distributions along the x-, y- and z-axes, respectively. Similar definitions apply for the three components $\mathbf{g}_m^x$, $\mathbf{g}_n^y$ and $\mathbf{g}_t^z$ of the gravity field.

In Eqs. (2) and (3), when $R \to 0$, a weak singularity of order $O(1/R)$ occurs for the gravity potential, and a strong singularity of order $O(1/R^2)$ needs to be handled in the computation of the gravitational acceleration. To start with, we deal with the x-component ϕ_m^x of the weakly singular gravity potential. By introducing an unit vector $\hat{\mathbf{x}} = \{1, 0, 0\}$ along the x-direction, we find that

$$\nabla_{\mathbf{r}} R = \frac{\mathbf{r} - \mathbf{r}'}{R}, \tag{6}$$

$$\hat{\mathbf{x}} \cdot \nabla_{\mathbf{r}} R = \frac{x}{R}, \tag{7}$$

$$x^{m-1} \hat{\mathbf{x}} \cdot \nabla_{\mathbf{r}} R = \frac{x^m}{R}, \tag{8}$$

where the assumption $\mathbf{r}' = (0, 0, 0)$ is used. Then, integrating the above Eq. (8) over the entire polyhedral body H, we have

$$\iiint_H (x^{m-1} \hat{\mathbf{x}} \cdot \nabla_{\mathbf{r}} R) \mathrm{d}v = \iiint_H \frac{x^m}{R} \mathrm{d}v. \tag{9}$$

Considering the definition of ϕ_m^x in Eq. (4), we get

$$\phi_m^x = \iiint_H (x^{m-1}\hat{\mathbf{x}} \cdot \nabla_{\mathbf{r}} R)\mathrm{d}v. \tag{10}$$

Similarly, we have the following expressions for ϕ_n^y and ϕ_t^z:

$$\phi_n^y = \iiint_H (y^{n-1}\hat{\mathbf{y}} \cdot \nabla_{\mathbf{r}} R)\mathrm{d}v, \tag{11}$$

$$\phi_t^z = \iiint_H (z^{t-1}\hat{\mathbf{z}} \cdot \nabla_{\mathbf{r}} R)\mathrm{d}v, \tag{12}$$

where $\hat{\mathbf{y}} = \{0, 1, 0\}$ and $\hat{\mathbf{z}} = \{0, 0, 1\}$ are the unit vectors along the y-axis and the z-axis, respectively.

Now, using these unit vectors $\hat{\mathbf{x}}$, $\hat{\mathbf{y}}$ and $\hat{\mathbf{z}}$, Eqs. (10)–(12) can be further simplified by using the following vector identity:

$$\chi\boldsymbol{\Psi} \cdot \nabla R + R\nabla \cdot (\chi\boldsymbol{\Psi}) = \nabla \cdot (R\chi\boldsymbol{\Psi}). \tag{13}$$

Setting $\boldsymbol{\Psi} = \hat{\mathbf{x}}$ and $\chi = x^{m-1}$, $\boldsymbol{\Psi} = \hat{\mathbf{y}}$ and $\chi = y^{n-1}$, and $\boldsymbol{\Psi} = \hat{\mathbf{z}}$ and $\chi = z^{t-1}$ in Eq. (13), and using the notation of $\nabla = \nabla_{\mathbf{r}}$, we have

$$x^{m-1}\hat{\mathbf{x}} \cdot \nabla R + R\nabla \cdot (x^{m-1}\hat{\mathbf{x}}) = \nabla \cdot (Rx^{m-1}\hat{\mathbf{x}}), \tag{14}$$

$$y^{n-1}\hat{\mathbf{y}} \cdot \nabla R + R\nabla \cdot (y^{n-1}\hat{\mathbf{y}}) = \nabla \cdot (Ry^{n-1}\hat{\mathbf{y}}), \tag{15}$$

$$z^{t-1}\hat{\mathbf{z}} \cdot \nabla R + R\nabla \cdot (z^{t-1}\hat{\mathbf{z}}) = \nabla \cdot (Rz^{t-1}\hat{\mathbf{z}}). \tag{16}$$

The surface ∂H of a polyhedral body is composed of N polygons, that is, $\partial H = \sum_{i=1}^{N} \partial H_i$. Substituting Eqs. (14), (15) and (16) into Eqs. (10), (11) and (12), respectively, and using the divergence theorem (Jin 2002), we get

$$\phi_m^x = \sum_{i=1}^{N} [\hat{\mathbf{n}}_i \cdot \hat{\mathbf{x}}] \iint_{\partial H_i} Rx^{m-1}\mathrm{d}s - (m-1) \iiint_H x^{m-2}R\mathrm{d}v, \tag{17}$$

$$\phi_n^y = \sum_{i=1}^{N} [\hat{\mathbf{n}}_i \cdot \hat{\mathbf{y}}] \iint_{\partial H_i} Ry^{n-1}\mathrm{d}s - (n-1) \iiint_H y^{n-2}R\mathrm{d}v, \tag{18}$$

$$\phi_t^z = \sum_{i=1}^{N} [\hat{\mathbf{n}}_i \cdot \hat{\mathbf{z}}] \iint_{\partial H_i} Rz^{t-1}\mathrm{d}s - (t-1) \iiint_H z^{t-2}R\mathrm{d}v, \tag{19}$$

in which $\mathbf{n}_i$ is the normal vector on polygon ∂H_i, $[\hat{\mathbf{n}}_i \cdot \hat{\mathbf{x}}]$, $[\hat{\mathbf{n}}_i \cdot \hat{\mathbf{y}}]$ and $[\hat{\mathbf{n}}_i \cdot \hat{\mathbf{z}}]$ are constant over polygon ∂H_i. We now deal with the above volume integral (note $\mathbf{r}' = (0, 0, 0)$):

$$
\begin{aligned}
H_{m-2,x,R} &= \iiint_H x^{m-2} R \mathrm{d}v \\
&= \iiint_H x^{m-2} \frac{1}{4} \nabla_{\mathbf{r}} \cdot [(\mathbf{r}-\mathbf{r}')R] \mathrm{d}v \\
&= \iiint_H \nabla_{\mathbf{r}} \cdot [x^{m-2} \frac{1}{4} (\mathbf{r}-\mathbf{r}')R] \mathrm{d}v - \iiint_H (\mathbf{r}-\mathbf{r}')R \cdot \nabla_{\mathbf{r}} (\frac{1}{4} x^{m-2}) \mathrm{d}v \\
&= \oiint_{\partial H} \frac{R x^{m-2}}{4} [(\mathbf{r}-\mathbf{r}') \cdot \mathbf{n}] \mathrm{d}s - \frac{(m-2)}{4} \iiint_H x^{m-2} R \mathrm{d}v \\
&= \sum_{i=1}^{N} \frac{-h_i}{4} \iint_{\partial H_i} x^{m-2} R \mathrm{d}s - \frac{m-2}{4} H_{m-2,x,R}.
\end{aligned}
\tag{20}
$$

Here, h_i is defined as $h_i = [(\mathbf{r}' - \mathbf{r}) \cdot \mathbf{n}_i]$, which is constant over the polygon ∂H_i, and $\mathbf{n}_i$ is the normal vector on polygon ∂H_i. Therefore, we have

$$
H_{m-2,x,R} = -\frac{1}{m+2} \sum_{i=1}^{N} h_i \iint_{\partial H_i} x^{m-2} R \mathrm{d}s. \tag{21}
$$

Similar results can be obtained for $H_{n-2,y,R}$ and $H_{t-2,z,R}$ in Eqs. (18) and (19), respectively. Now, we observe that the original expression for the total gravity potential ϕ in Eq. (4) with a weak singularity of $O(1 / R)$ was successfully transformed to regular surface integrals of the form $O(R)$ in Eqs. (17)–(19). This means that even when no analytic formulae exist for the gravity potential $\phi_{mnt} = -G(a\phi_m^x + b\phi_n^y + c\phi_t^z)$ with high orders, standard quadrature rules can still be easily adopted to evaluate the gravity potential with high accuracy.

2.1.2 Gravitational Acceleration

Now, we proceed to the gravity field terms $\mathbf{g}_m^x$, $\mathbf{g}_n^y$ and $\mathbf{g}_t^z$ with strong singularities of order $O(1/R^2)$. Since most gravimeters can only measure the vertical component of the gravity field, here, we only discuss the formula to compute the vertical component of the gravity field along the positive z-axis. The formulae to compute the other components along the horizontal x- and y-axes can be derived in a similar way. For simplicity, we use the scalar symbols g_m^x, g_n^y and g_t^z to denote the vertical components of $\mathbf{g}_m^x$, $\mathbf{g}_n^y$ and $\mathbf{g}_t^z$. The first step is to transform the strong singularities into weak ones of order $O(1 / R)$ by using the vector identity of Eq. (13) where we assign the unit z-axis vector $\hat{\mathbf{z}}$ to the arbitrary vector $\boldsymbol{\Psi}$, set $\chi = x^m, y^n, z^t$, and replace R by $\frac{1}{R}$:

$$
x^m \hat{\mathbf{z}} \cdot \nabla \frac{1}{R} + \frac{1}{R} \nabla \cdot (x^m \hat{\mathbf{z}}) = \nabla \cdot \left(x^m \hat{\mathbf{z}} \frac{1}{R} \right), \tag{22}
$$

$$
y^n \hat{\mathbf{z}} \cdot \nabla \frac{1}{R} + \frac{1}{R} \nabla \cdot (y^n \hat{\mathbf{z}}) = \nabla \cdot \left(y^n \hat{\mathbf{z}} \frac{1}{R} \right), \tag{23}
$$

$$
z^t \hat{\mathbf{z}} \cdot \nabla \frac{1}{R} + \frac{1}{R} \nabla \cdot (z^t \hat{\mathbf{z}}) = \nabla \cdot \left(z^t \hat{\mathbf{z}} \frac{1}{R} \right). \tag{24}
$$

This yields

$$g_m^x = \iiint_H x^m \hat{\mathbf{z}} \cdot \nabla \frac{1}{R} \mathrm{d}v = \iiint_H \nabla \cdot (x^m \frac{1}{R} \hat{\mathbf{z}}) \mathrm{d}v - \iiint_H \frac{1}{R} \nabla \cdot (x^m \hat{\mathbf{z}}) \mathrm{d}v, \tag{25}$$

$$g_n^y = \iiint_H y^n \hat{\mathbf{z}} \cdot \nabla \frac{1}{R} \mathrm{d}v = \iiint_H \nabla \cdot (y^n \frac{1}{R} \hat{\mathbf{z}}) \mathrm{d}v - \iiint_H \frac{1}{R} \nabla \cdot (y^n \hat{\mathbf{z}}) \mathrm{d}v, \tag{26}$$

$$g_t^z = \iiint_H z^t \hat{\mathbf{z}} \cdot \nabla \frac{1}{R} \mathrm{d}v = \iiint_H \nabla \cdot (z^t \frac{1}{R} \hat{\mathbf{z}}) \mathrm{d}v - \iiint_H \frac{1}{R} \nabla \cdot (z^t \hat{\mathbf{z}}) \mathrm{d}v. \tag{27}$$

Using the divergence theorem (Jin 2002), we get

$$g_m^x = \sum_{i=1}^{N} [\hat{\mathbf{z}} \cdot \mathbf{n}_i] \iint_{\partial H_i} \frac{x^m}{R} \mathrm{d}s, \tag{28}$$

$$g_n^y = \sum_{i=1}^{N} [\hat{\mathbf{z}} \cdot \mathbf{n}_i] \iint_{\partial H_i} \frac{y^n}{R} \mathrm{d}s, \tag{29}$$

$$g_t^z = \sum_{i=1}^{N} [\hat{\mathbf{z}} \cdot \mathbf{n}_i] \iint_{\partial H_i} \frac{z^t}{R} \mathrm{d}s - t\phi_{t-1}^z, \tag{30}$$

in which $\mathbf{n}_i$ is the normal vector on polygon ∂H_i, $[\hat{\mathbf{z}} \cdot \hat{\mathbf{n}}_i]$ is constant over polygon ∂H_i, and ϕ_{t-1}^z is the gravity potential caused by a depth-dependent mass density contrast of order $\lambda(\mathbf{r}) = z^{t-1}$ (see Eq. 4 for its definition). In the above equations, the original strong singularity of $O(1/R^2)$ in the vertical gravity field $g_{mnt} = -G(ag_m^x + bg_n^y + cg_t^z)$ was reduced by one order to a weak singularity of form $O(1 / R)$.

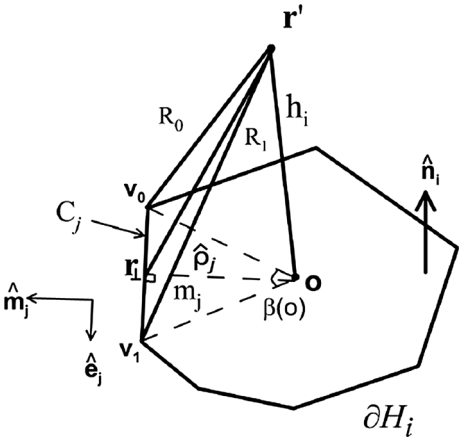

Fig. 1 Illustration of the geometrical relationship between the observation site $\mathbf{r}'$ and an edge C_j of a polygon ∂H_i. The point $\mathbf{o}$ is the projection point of $\mathbf{r}'$ onto the polygon ∂H_i

2.2 Closed-form Solutions for Surface Integrals and Final Singularity Removal

In Eqs. (17)–(19) and (28)–(30), we need to evaluate surface integrals of the form $\iint_{\partial H_i} f^k R^q \mathrm{d}s$ where f is either x, y or z, k is an integer, and $q = -1, 1$. If $q = -1$ and $R \to 0$, the surface integral has a singular integrand.

To remove the possible singularity, we set up a local polar coordinate system (ρ, ϕ) on the polygon ∂H_i. As shown in Fig. 1, we first project the observation site $\mathbf{r}'$ onto the plane ∂H_i with the projection point denoted by point $\mathbf{o}$. The extent angle at point $\mathbf{o}$ is $\beta(\mathbf{o}) = \sum_j \beta(\mathbf{o})_j$, where $\beta(\mathbf{o})_j$ is the angular extent of the arc edge C_j or the solid angle (Wilton et al. 1984; Werner 1994), the tangential vector of edge C_j is denoted by $\hat{\mathbf{e}}_j$ and $\hat{\mathbf{m}}_j$ is the normal vector of edge C_j, $\hat{\mathbf{n}}_i$ is the normal vector of polygon ∂H_i, and $\hat{\mathbf{m}}_j \times \hat{\mathbf{e}}_j = \hat{\mathbf{n}}_i$. h_i is the height of the site $\mathbf{r}'$ above the polygon ∂H_i, i.e., $h_i = (\mathbf{r}' - \mathbf{r}) \cdot \hat{\mathbf{n}}_i$. Edge C_j is parametrized by a single variable s, $s = (\mathbf{r} - \mathbf{o}) \cdot \hat{\mathbf{e}}_j$, s_0 and s_1 are the parametrized coordinates of two vertices v_0 and v_1 of edge C_j, R_0 and R_1 are the distances from point $\mathbf{r}'$ to the vertices v_0 and v_1, respectively. The distance from the source point $\mathbf{r} \in \partial H_i$ to the coordinate center $\mathbf{o}$ is $\rho = |\mathbf{r} - \mathbf{o}|$. Hence, the distance from the site $\mathbf{r}'$ to the source point $\mathbf{r}$ becomes $R = |\mathbf{r}' - \mathbf{r}| = \sqrt{(h_i^2 + \rho^2)}$. The term f^k could be a complicated function over the polygon; in this study, we derived closed forms only for cases of $k = 0, -1$.

First, we have the following identity:

$$R^q = \nabla_s \cdot \frac{1}{q+2} \frac{R^{q+2}}{\rho^2} (\mathbf{r} - \mathbf{o}), \tag{31}$$

in which ∇_s denotes the surface divergence operation in the local coordinates of the plane.

Proof Instead of using the local polar coordinate system, here a local 2D Cartesian coordinate system (u, v) is used. Then, assuming u and v are the local coordinates of point $\mathbf{r}$, (0, 0) is the 2D local coordinate center $\mathbf{o}$, $R = \sqrt{(u^2 + v^2 + h_i^2)}$, and $\rho = \sqrt{u^2 + v^2}$, we have

$$\begin{aligned}
\nabla_s \cdot \frac{1}{q+2} \frac{R^{q+2}}{\rho^2} (\mathbf{r} - \mathbf{o}) &= \frac{1}{q+2} \left\{ \frac{\partial}{\partial u} \left(\frac{R^{q+2}}{\rho^2} u \right) + \frac{\partial}{\partial v} \left(\frac{R^{q+2}}{\rho^2} v \right) \right\} \\
&= \frac{1}{q+2} \left\{ \frac{(q+2) R^{q+1} \frac{u}{R} \rho^2 - R^{q+2} 2\rho \frac{u}{\rho}}{\rho^4} u \right. \\
&\quad \left. + \frac{(q+2) R^{q+1} \frac{v}{R} \rho^2 - R^{q+2} 2\rho \frac{v}{\rho}}{\rho^4} v + 2 \frac{R^{q+2}}{\rho^2} \right\} \\
&= \frac{1}{q+2} \left\{ \frac{q+2}{\rho^4} R^q \rho^4 - \frac{2R^{q+2}}{\rho^4} \rho^2 + 2 \frac{R^{q+2}}{\rho^2} \right\} \\
&= R^q.
\end{aligned} \tag{32}$$

□

Second, to deal with the weak singularity occurring for $R \to 0$, the surface ∂H_i is divided into two regions, one circular region $\bigcirc_\epsilon$ centered at point $\mathbf{o}$ with an infinitely small radius $\epsilon \to 0$, and the remaining region $\partial H_i - \bigcirc_\epsilon$. Hence, for the case $k = 0$,

$$
\begin{aligned}
I_{R^q} = \iint_{\partial H_i} R^q \mathrm{d}s &= \frac{1}{q+2} \iint_{\partial H_i - \bigcirc_\epsilon} \nabla_s \cdot \left(\frac{R^{q+2}}{\rho^2} (\mathbf{r} - \mathbf{o}) \right) \mathrm{d}s + \iint_{\bigcirc_\epsilon} R^q \mathrm{d}s \\
&= \frac{1}{q+2} \sum_{j=1}^{M} m_j \int_{C_j} \frac{R^{q+2}}{\rho^2} \mathrm{d}l - \frac{1}{q+2} \frac{\left(\sqrt{h_i^2 + \epsilon^2} \right)^{q+2}}{\epsilon} \int_{\partial \bigcirc_\epsilon} \mathrm{d}l \\
&\quad + \int_0^{\beta(\mathbf{o})} \int_0^{\epsilon} \rho (\sqrt{h_i^2 + \rho^2})^q \mathrm{d}\rho \mathrm{d}\phi \\
&= \frac{1}{q+2} \sum_{j=1}^{M} m_j \int_{C_j} \frac{R^{q+2}}{\rho^2} \mathrm{d}l - \frac{1}{q+2} \frac{\left(\sqrt{h_i^2 + \epsilon^2} \right)^{q+2}}{\epsilon} \epsilon \int_0^{\beta(\mathbf{o})} \mathrm{d}\phi \\
&\quad + \frac{\beta(\mathbf{o})}{q+2} (\sqrt{h_i^2 + \rho^2})^{q+2} |_o^{\epsilon} \\
&= \frac{1}{q+2} \sum_{j=1}^{M} m_j \int_{C_j} \frac{R^{q+2}}{\rho^2} \mathrm{d}l \\
&\quad - \frac{\beta(\mathbf{o})}{q+2} \left(\sqrt{h_i^2 + \epsilon^2} \right)^{q+2} + \frac{\beta(\mathbf{o})}{q+2} \left(\sqrt{h_i^2 + \epsilon^2} \right)^{q+2} - \frac{\beta(\mathbf{o})}{q+2} |h_i|^{q+2} \\
&= \frac{1}{q+2} \sum_{j=1}^{M} m_j \int_{C_j} \frac{R^{q+2}}{\rho^2} \mathrm{d}l - \frac{\beta(\mathbf{o})}{q+2} |h_i|^{q+2} \\
&= \frac{1}{q+2} \sum_{j=1}^{M} B_j^{q+2} - \frac{\beta(\mathbf{o})}{q+2} |h_i|^{q+2},
\end{aligned}
\tag{33}
$$

where, referring to Fig. 1, $m_j = (\mathbf{r} - \mathbf{o}) \cdot \hat{\mathbf{m}}_j$ is constant over edge C_j, $\hat{\mathbf{m}}_j$ is the normal vector on edge C_j, and $\beta(\mathbf{o})$ is the solid angle of $\bigcirc_\epsilon$ centered at point $\mathbf{o}$ in the plane ∂H_i (see Eq. 48 in the "Appendix" for its calculation). We also note that when point $\mathbf{o}$ is located at a corner or on an edge, the respective distance term m_j vanishes. In the above, we defined a new term $B_j^{q+2} = m_j \int_{C_j} \frac{R^{q+2}}{\rho^2} \mathrm{d}l$ which will be considered in the "Appendix".

Third, for the surface integrals of form $\iint_{\partial H_i} f^k R^q \mathrm{d}s$ in Eqs. (17)–(19) and (28)–(30) and $k = 1$, we retrieve

$$
\begin{aligned}
\mathbf{I}_{rR_q} = \iint\limits_{\partial H_i} \mathbf{r}R^q \mathrm{d}s &= (\mathbf{o}-\mathbf{r}') \iint\limits_{\partial H_i} R^q \mathrm{d}s + \iint\limits_{\partial H_i} (\mathbf{r}-\mathbf{o})R^q \mathrm{d}s \\
&= (\mathbf{o}-\mathbf{r}')I_{R^q} + \iint\limits_{\partial H_i - \bigcirc_\epsilon} \nabla_s \left(\frac{R^{q+2}}{q+2}\right) \mathrm{d}s + \iint\limits_{\bigcirc_\epsilon} (\mathbf{r}-\mathbf{o})R^q \mathrm{d}s \\
&= (\mathbf{o}-\mathbf{r}')I_{R^q} + \frac{1}{q+2}\sum_{j=1}^{M} \hat{\mathbf{m}}_j \int_{C_j} R^{q+2} \mathrm{d}l \\
&\quad + \frac{(\sqrt{h^2+\epsilon^2})^{q+2}}{q+2} \oiint\limits_{\partial \bigcirc_\epsilon} \hat{\mathbf{m}}_j \mathrm{d}l + \int_0^{\beta(\mathbf{o})} \int_0^{\epsilon} \hat{\boldsymbol{\rho}} \rho^2 R^q \mathrm{d}\rho \mathrm{d}\phi \\
&\overset{\epsilon \to 0}{=} (\mathbf{o}-\mathbf{r}')I_{R^q} + \frac{1}{q+2}\sum_{j=1}^{M} \hat{\mathbf{m}}_j \int_{C_j} R^{q+2} \mathrm{d}l \\
&= (\mathbf{o}-\mathbf{r}')I_{R^q} + \frac{1}{q+2}\sum_{j=1}^{M} \mathbf{B}_j^{q+2},
\end{aligned}
\tag{34}
$$

where the term $\hat{\mathbf{m}}_j \int_{C_j} R^{q+2} \mathrm{d}l$ is denoted by a new variable $\mathbf{B}_j^{q+2}$ and $\hat{\boldsymbol{\rho}}$ is a unit vector pointing from point $\mathbf{o}$ to point $\mathbf{r}$. Note that we have used $\mathbf{r} = (x, y, z) = \mathbf{r} - \mathbf{r}' = \mathbf{r} - \mathbf{o} + \mathbf{o} - \mathbf{r}'$, where the assumption $\mathbf{r}' = (0, 0, 0)$ is used. The term I_{R^q} is given in Eq. (33), and the following identity is used:

$$
(\mathbf{r}-\mathbf{o})R^q = \nabla_s \left(\frac{R^{q+2}}{q+2}\right).
$$

To compute the gravity potential and the gravity field, we only have to deal with the cases of $q = -1, 1$. Note, analytic formulae for the scalar term B_j^{q+2} and the vector term $\mathbf{B}_j^{q+2}$ in Eqs. (33) and (34), respectively, are given in the "Appendix" for the cases $q = -1$ and $q = 1$.

2.3 Special Cases

2.3.1 Zeroth-Order Density Variation

For $m = n = t = 0$, i.e., spatially homogeneous density, Eq. (4) simplifies to

$$
\phi_0^x = \phi_0^y = \phi_0^z = \iiint\limits_H \frac{1}{R} \mathrm{d}v. \tag{35}
$$

Substituting the vector identity (Hamayun and Tenzer 2009)

$$
\frac{1}{R} = \frac{1}{2} \nabla_{\mathbf{r}} \cdot \frac{\mathbf{r}-\mathbf{r}'}{R}
$$

into Eq. (35) gives

$$
\phi_{000} = \frac{G(a+b+c)}{2} \iiint\limits_H \nabla_{\mathbf{r}} \cdot \frac{\mathbf{r}-\mathbf{r}'}{R} \mathrm{d}v = -\frac{G(a+b+c)}{2} \sum_{i=1}^{N} h_i \iint\limits_{\partial H_i} \frac{1}{R} \mathrm{d}s, \tag{36}
$$

where the divergence theorem (Jin 2002) was used. The term $h_i = (\mathbf{r}' - \mathbf{r}) \cdot \hat{\mathbf{n}}_i$ for $\mathbf{r} \in \partial H_i$ is the normal distance from the observation site $\mathbf{r}'$ to the surface ∂H_i along the direction of $\hat{\mathbf{n}}_i$, here $\hat{\mathbf{n}}_i$ is the outgoing surface normal vector (Fig. 1). Setting $m = n = t = 0$ in Eqs. (28)–(30), we have

$$g_{000} = -G \sum_{i=1}^{N} \{(a+b+c)[\hat{\mathbf{n}}_i \cdot \hat{\mathbf{z}}]\} \iint_{\partial H_i} \frac{1}{R} \mathrm{d}s. \tag{37}$$

Therefore, by setting $q = -1$ in Eq. (33), singularity-free analytic expressions for the gravity potential and the gravity field of a homogeneous polyhedral body are developed.

2.3.2 First-Order Density Variation

Now we consider the linear case of $\lambda(\mathbf{r}) = \mathbf{A} \cdot \mathbf{r}$, $\mathbf{A} = (a, b, c)$ and $\mathbf{r} = (x, y, z)$. Setting $m = n = t = 1$ in Eqs. (17), (18) and (19), we have

$$\phi_{111} = \sum_{i=1}^{N} \{a[\hat{\mathbf{n}}_i \cdot \hat{\mathbf{x}}] + b[\hat{\mathbf{n}}_i \cdot \hat{\mathbf{y}}] + c[\hat{\mathbf{n}}_i \cdot \hat{\mathbf{z}}]\} \iint_{\partial H_i} R \mathrm{d}s. \tag{38}$$

Similarly, setting $m = n = t = 1$ in Eqs. (28)–(30) yields

$$g_{111} = -G \sum_{i=1}^{N} [\hat{\mathbf{n}}_i \cdot \hat{\mathbf{z}}] \mathbf{A} \cdot \iint_{\partial H_i} \mathbf{r} R^{-1} \mathrm{d}s + cG\phi_0^z. \tag{39}$$

Setting $q = 1$ in Eq. (33) and $q = -1$ in Eq. (34), the singularity-free analytic expressions for ϕ_{111} and g_{111} are obtained.

2.3.3 Second-Order Density Variation

Setting $m = 2, n = 2, t = 2$, the terms for the gravitational potential in Eqs. (17)–(21) simplify to integrals of the forms $\iint_{\partial H_i} \mathbf{r} R \mathrm{d}s$ and $\iint_{\partial H_i} R \mathrm{d}s$. These expressions can be analytically integrated using $q = 1$ in Eqs. (33) and (34), and hence, the gravity potential ϕ has closed forms. However, for the gravity field, closed forms cannot be derived using the formulae in Eqs. (33) and (34).

2.3.4 Comparison of Available Solutions for Zeroth- to Second-Order Density Variations

In Table 1, we have listed the currently available closed-form solutions for a general polyhedral mass body with constant, linear or quadratic polynomial mass density. Recently, D'Urso (2013, 2014a) has used the distribution theory to derive closed-form solutions for a constant polyhedron and have discussed a way of eliminating singularities. Subsequently, D'Urso (2014b) extended the distribution theory on a general polyhedron with linear mass polynomials. Conway (2015) has employed a vector potential technique to derive closed-form solutions for a constant polyhedron. Compared to these techniques, our approaches have adopted a simple generalized framework to deal with constant and linear cases. To our best knowledge, our new equations are the first to deliver closed-form

Table 1 Comparison of our closed-form solution to other available closed-form solutions for a general polyhedral mass body

General 3D polyhedra			
Density contrast	Singularity-free	Components	References
Constant	–	g^z	Paul (1974)
Constant	–	g^z, ϕ	Barnett (1976)
Constant	–	$\nabla\phi$, $\nabla\nabla\phi$	Okabe (1979)
Constant	√	ϕ	Waldvogel (1979)
Constant	√	$\nabla\phi$	Pohanka (1988)
Constant	√	$\nabla\nabla\phi$	Kwok (1991)
Constant	√	$\nabla\phi$	Holstein and Ketteridge (1996)
Constant	√	ϕ, $\nabla\phi$, $\nabla\nabla\phi$	D'Urso (2013, 2014a)
Constant	√	$\nabla\phi$	Conway (2015)
Linear	√	$\nabla\phi$	Hansen (1999)
Linear	√	ϕ, $\nabla\phi$, $\nabla\nabla\phi$	Holstein (2003)
Linear	√	ϕ	Hamayun and Tenzer (2009)
Linear	√	ϕ, $\nabla\phi$, $\nabla\nabla\phi$	D'Urso (2014b)
Constant	√	ϕ, $\nabla\phi$	Our approach
Linear	√	ϕ, $\nabla\phi$	Our approach
Quadratic	√	ϕ	Our approach

Symbols √ and – indicate the availability and non-availability of a singularity-free analytic formula. Symbol ϕ denotes the gravitational potential, $\nabla\phi$ denotes the gravitational field and $\nabla\nabla\phi$ denotes the gravity gradient tensor (e.g., Beiki and Pedersen 2010; Abtahi et al. 2016)

solutions for the gravitational potential of a general polyhedral body with quadratic density contrast varying in all spatial directions.

2.3.5 A Regular Prismatic Body

The surface of a prismatic body is composed of six rectangular surfaces $\diamondsuit_i$, that is, $\partial H = \sum_{i=1}^{6} \diamondsuit_i$. In a 3D Cartesian coordinate system with the positive z-axis downward, we arrange the rectangular surfaces as follows: (1) $\diamondsuit_1$ and $\diamondsuit_2$ are the two rectangular surfaces perpendicular to the x-axis where the x-coordinate of plane $\diamondsuit_1$ is less than that of plane $\diamondsuit_2$; (2) $\diamondsuit_3$ and $\diamondsuit_4$ are the two rectangular surfaces perpendicular to the y-axis where the y-coordinate of plane $\diamondsuit_3$ is less than that of plane $\diamondsuit_4$; and (3) $\diamondsuit_5$ and $\diamondsuit_6$ are the two rectangular surfaces perpendicular to the z-axis where the z-coordinate of plane $\diamondsuit_5$ is less than that of plane $\diamondsuit_6$. With this choice, the terms of the gravity potential in Eqs. (17)–(21) become

$$\phi_m^x = \sum_{i=1}^{2} (-1)^i x_{\diamondsuit_i}^{m-1} \iint_{\diamondsuit_i} R \mathrm{d}s + \frac{m-1}{m+2} \sum_{i=1}^{6} h_i \iint_{\diamondsuit_i} x^{m-2} R \mathrm{d}s, \tag{40}$$

$$\phi_n^y = \sum_{i=3}^{4}(-1)^i y_{\diamond_i}^{n-1} \iint\limits_{\diamond_i} R\mathrm{d}s + \frac{n-1}{n+2}\sum_{i=1}^{6} h_i \iint\limits_{\diamond_i} y^{n-2} R\mathrm{d}s, \tag{41}$$

$$\phi_t^z = \sum_{i=5}^{6}(-1)^i z_{\diamond_i}^{t-1} \iint\limits_{\diamond_i} R\mathrm{d}s + \frac{t-1}{t+2}\sum_{i=1}^{6} h_i \iint\limits_{\diamond_i} z^{t-2} R\mathrm{d}s, \tag{42}$$

and the vertical gravity field in Eqs. (28)–(30) consists of the terms

$$g_m^x = \sum_{i=5}^{6}(-1)^i \iint\limits_{\diamond_i} \frac{x^m}{R}\mathrm{d}s, \tag{43}$$

$$g_n^y = \sum_{i=5}^{6}(-1)^i \iint\limits_{\diamond_i} \frac{y^n}{R}\mathrm{d}s, \tag{44}$$

$$g_t^z = \sum_{i=5}^{6}(-1)^i z_{\diamond_i}^t \iint\limits_{\diamond_i} \frac{1}{R}\mathrm{d}s - t\phi_{t-1}^z. \tag{45}$$

Considering Eqs. (40)–(42) and (33)–(34), and the results discussed in the above special cases, we find that, when $m \le 3, n \le 3, t \le 3$, all three terms of the gravity potential have analytic expressions. However, based on the results given in Eqs. (33)–(34), closed forms can be derived only if $m \le 1, n \le 1$ for the g_m^x and g_n^y terms of the gravity field. Since ϕ_{t-1}^z has closed forms in the case of $t-1 \le 3$, g_t^z has closed forms if $t \le 4$. These results for a prismatic body are shown in Table 2 for reference.

As shown in Table 2, for a prismatic body with constant, linear, quadratic and cubic density contrasts varying in both horizontal and vertical directions, our approach can deliver closed-form solutions for the gravitational potential. For the gravitational field, closed-form solutions exist in the cases of constant and linear density contrasts. Compared to previously published methods (Nagy et al. 2000; Rao 1990; García-Abdeslem 2005), one novelty of our approach is that our closed-form solutions are singularity-free which means the observation sites can be outside, inside and on the boundary (edges, corners, faces) of the mass prismatic body.

Table 2 Lookup table for the availability of analytic formulae of the gravity potential (terms ϕ_m^x, ϕ_n^y, ϕ_t^z in Eqs. 40–42) and the vertical gravity field (terms g_m^x, g_n^y, g_t^z in Eqs. 43–45) for a prismatic body

Order	ϕ_m^x	ϕ_n^y	ϕ_t^z	g_m^x	g_n^y	g_t^z
0	√	√	√	√	√	√
1	√	√	√	√	√	√
2	√	√	√			√
3	√	√	√			√
4						√

Symbol √ indicates the existences of an analytic formula

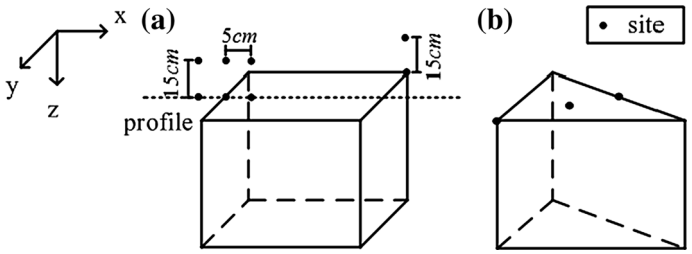

Fig. 2 García-Abdeslem's (2005) prism model (**a**). A triangular prism model (**b**) is constructed from García-Abdeslem's (2005) prism model with half the volume. *Black dots* represent observation sites

3 Verification

Two synthetic models (as shown in Fig. 2) are used to verify the accuracies of our closed-form solutions. The global Cartesian coordinate system is used to describe the geometries of these two models and locations of testing sites and profiles. Our closed-form formulae use the assumption that the observation site is located at the coordinate origin. Therefore, to compute the gravity signals in these two synthetic models, a coordinate transform from the global Cartesian coordinate system to the local Cartesian coordinate system is needed at each observation site by our closed-form formulae to guarantee that it is at the local coordinate origin.

3.1 A Prismatic Body with Vertically Varying Density Contrast

To validate our new singularity-free analytic formulae, first the popular prismatic model is tested. Four different depth-dependent polynomial density contrasts are examined, which are the constant, linear, quadratic and cubic variations. A Cartesian coordinate system is defined in a way that the positive z-axis is downward. The dimension of the prismatic body is $x = [10\,\text{km}, 20\,\text{km}]$, $y = [10\,\text{km}, 20\,\text{km}]$ and $z = [0\,\text{km}, 8\,\text{km}]$ (Fig. 2a). The density contrast function, which is taken from a previous work (García-Abdeslem 2005), is given as:

$$\lambda(\mathbf{r}) = -747.7 + 203.435z - 26.764z^2 + 1.4247z^3 \tag{46}$$

where density is in kg/m^3 and z is in km. When the observation site approaches the prism, i.e., the edges, surfaces or corners of the prism, the gravity potential and the gravity field become singular. In the previous work (García-Abdeslem 2005), analytic formulae for depth-dependent density contrasts up to third order were derived. However, these analytic formulae are singular when the observation sites are located on edges or corners.

First, a short measuring profile with three observation sites is arranged on the top surface of the prism, which is perpendicular to an edge with $x = 10\,\text{km}, z = 0\,\text{km}$. When the profile is slightly more elevated (with $z = -0.15\,\text{m}$), the singularity disappears so that we can compare the accuracies of our analytic solutions against the closed-form solutions, which were recomputed by the formula offered by García-Abdeslem (2005). This accuracy comparison for the regular case is shown in Table 3, and an excellent agreement is obtained between these two different closed-form solutions. A slight difference appears at the 14-th significant digit, which is close to the machine precision limitations of the computer. When setting $z = 0\,\text{km}$ for the profile as shown in Table 4, a singularity in

Table 3 Comparison of the vertical gravity field (g_{00t}) computed by our analytic solutions and García-Abdeslem's (2005) closed-form solutions for the prism model shown in Fig. 2a

Order	g_{00t} along profile ($z = -0.15$ m, $y = 15$ km)		
	x (km)	Our closed-form solutions (mGal)	García-Abdeslem's solutions (mGal)
Constant ($t = 0$)	9.99995	−7.00101521434592E+001	−7.00101521434591E+001
	10	−7.00153407823801E+001	−7.00153407823800E+001
	10.00005	−7.00641689787295E+001	−7.00641689787295E+001
Linear ($t = 1$)	9.99995	5.97357825457560E+001	5.97357825457560E+001
	10	5.97365628358933E+001	5.97365628358932E+001
	10.00005	5.97443654585579E+001	5.97443654585579E+001
Quadratic ($t = 2$)	9.99995	−3.69173288088277E+001	−3.69173288088277E+001
	10	−3.69176741955519E+001	−3.69176741955519E+001
	10.00005	−3.69211280340700E+001	−3.69211280340700E+001
Cubic ($t = 3$)	9.99995	1.09299348988834E+001	1.09299348988833E+001
	10	1.09300234258250E+001	1.09300234258250E+001
	10.00005	1.09309086860681E+001	1.09309086860681E+001

The measuring profile has a vertical coordinate of $z = -0.15$ m and approaches the edge ($x = 10$ km, $z = 0$ km) of the prism. Differences between the solutions are shown in bold face

Table 4 Comparison of the vertical gravity field (g_{00t}) between our analytic solutions and García-Abdeslem's (2005) closed-form solutions for the prism model shown in Fig. 2a

Order	g_{00t} along profile ($z = 0$ km, $y = 15$ km)		
	x (km)	Our closed-form solutions (mGal)	García-Abdeslem's solution (mGal)
Constant ($t = 0$)	9.99995	−7.00108086223439E+001	−7.00108086223439E+001
	10	−7.00170532866468E+001	–
	10.00005	−7.00680113760199E+001	−7.00680113760199E+001
Linear ($t = 1$)	9.99995	5.97372496760186E+001	5.97372496760185E+001
	10	5.97380301857833E+001	–
	10.00005	5.97458347641883E+001	5.97458347641883E+001
Quadratic ($t = 2$)	9.99995	−3.69182233831518E+001	−3.69182233831518E+001
	10	−3.69185687923601E+001	–
	10.00005	−3.69220228557056E+001	−3.69220228557055E+001
Cubic ($t = 3$)	9.99995	1.09301961657224E+001	1.09301961657224E+001
	10	1.09302846973961E+001	–
	10.00005	1.09311700049598E+001	1.09311700049598E+001

The measuring profile crosses the edge ($x = 10$ km, $z = 0$ km) of the prism. Symbol (–) indicates no solution available. Differences between the solutions are shown in bold face

García-Abdeslem's (2005) formulae at the edge (at $x = 10$ km) impedes computation of a solution [indicated by symbol (–)]. Instead, a smooth solution is obtained by our singularity-free analytic formulae. As observed from Table 4, the smooth transition of our computed vertical gravity field g_{00t} across the edge implies the correctness of the solution when the observation sites are located on the edge.

Secondly, we performed another test, where the observation site is located at one of the corners on the top surface of the prism. Due to the model symmetry, the gravity anomalies at the four top corners have the same values. Therefore, only the case of one corner ($x = 20\,\text{km}, y = 10\,\text{km}, z = 0\,\text{km}$) is considered. Similar to the above test, a location at slightly higher elevation (with $z = -0.15\,\text{m}$) is required for García-Abdeslem's (2005) analytic expressions. The comparison between our solutions and García-Abdeslem's solutions is shown in Table 5. Apparently, these two different solutions are identical up to the 14-th significant digit. In the singular case (see Table 6) where the observation site is coincident with the corner, our solutions still show smooth results with respect to the above solutions with a slightly more elevated observation site, implying the correctness of our formulae.

3.2 A Polyhedral Body with Constant Density Contrast

To test the performance of our closed-form approach in the case of arbitrary polyhedral bodies, a complicated triangular prism is selected as shown in Fig. 2b. The triangular prism has half the volume of the prism (cutting in halves the original prism along diagonals of the top and bottom surfaces) and has a mass density of $2670\,\text{kg/m}^3$; only the vertical gravity fields are computed. The triangular surface has a size of $\frac{1}{2} \times 10\,\text{km} \times 10\,\text{km}$. Three observation sites are located on the top triangular surface of the anomaly, one at a vertex, one at the mid point of an edge and one at the center of the surface. Hence, singularities might exist.

When the observation site is located at the diagonal edge as shown in Fig. 2b, the vertical gravity field caused by the triangular prism has half the value of that caused by the prismatic body, due to geometrical symmetries. Therefore, half the value of the well-established Gbox solution (Blakely 1996) can be used as reference. Additionally, the analytic solutions with linear integrals for arbitrary polyhedral bodies from Tsoulis (2012) are also taken as references. The test results are given in Table 7; they show that, using our closed-form formula, the computed g_z of the triangular prism is exactly a factor of 0.5 of g_z caused by the prismatic body. Our closed-form solution has an excellent agreement with that computed by the Gbox code (up to the 15-th significant digit). There is a negligible difference (after the 7-th significant digit) between our closed-form solution and Tsoulis's (2012) solution. Similar deviations also are observed for the cases that the observation sites

Table 5 Comparison of the vertical gravity field (g_{00t}) between our analytic solutions and García-Abdeslem's (2005) closed-form solutions for the prism model shown in Fig. 2a

Order	g_{00t} at point ($x = 20\,\text{km}, y = 10\,\text{km}, z = -0.15\,\text{m}$)	
	Our closed-form solutions (mGal)	García-Abdeslem's solution (mGal)
Constant ($t = 0$)	−4.25105387729770E+001	−4.25105387729770E+001
Linear ($t = 1$)	3.95707907656690E+001	3.95707907656692E+001
Quadratic ($t = 2$)	−2.55689100895767E+001	−2.55689100895767E+001
Cubic ($t = 3$)	7.76642695050040E+000	7.76642695050040E+000

The measuring point is located at a point very close to the top corner of the prism. The vertical coordinate of the considered top corner is $x = 20\,\text{km}, y = 10\,\text{km}, z = 0\,\text{km}$. Differences between the solutions are shown in bold face

Table 6 Comparison of the vertical gravity field (g_{00t}) between our analytic solutions and García-Abdeslem's (2005) closed-form solutions for the prism model shown in Fig. 2a

Order	g_{00t} at corner ($x = 20\,\text{km}, y = 10\,\text{km}, z = 0\,\text{km}$)	
	Our closed-form solutions (mGal)	García-Abdeslem's solution (mGal)
Constant ($t = 0$)	−4.25112235972466E+001	–
Linear ($t = 1$)	3.95714574971360E+001	–
Quadratic ($t = 2$)	−2.55693475942219E+001	–
Cubic ($t = 3$)	7.76656065625613E+000	–

The observation point is located at the top corner of the prism. Symbol (–) indicates no solution available

Table 7 Comparisons of the vertical gravity field computed by our closed-form formula to other approaches for the triangular prism model as shown in Fig. 2b

Locations	Methods	g_z (mGal)
Middle edge	Our formula	2.142578**084292794**E+002
	Tsoulis (2012)'s formula	2.142578**361848591**E+002
	$\frac{1}{2}\times$ GBOX's formula for prism	2.142578**084292798**E+002
	$\frac{1}{2}\times$ Our formula for prism	2.142578**084292794**E+002
Vertices	Our formula	1.302013**719579445**E+002
	Tsoulis (2012)'s formula	1.302013**874827574**E+002
Face centre	Our formula	3.255085**457339834**E+002
	Tsoulis (2012)'s formula	3.255085**967044333**E+002

Differences between the solutions are shown in bold face

are located at the vertex and the center of the surface. The differences between the different solutions are well below instrumental accuracy (0.002–0.010 mGal), demonstrating the generally high accuracy of the compared algorithms.

3.3 A Prismatic Body with Quartic Density Contrast

Additionally, we calculate the gravity acceleration for a prismatic body with a quartic density contrast which is

$$\lambda(\mathbf{r}) = z^4. \tag{47}$$

The profile is along the top surface of the prismatic body ($y = 5\,\text{km}$ and $z = 0\,\text{km}$) as shown in Fig. 2a. The reference solutions are calculated by the high-order Gaussian quadrature rule with $512 \times 512 \times 512$ quadrature points. As the quadrature points are located inside the prismatic body, solutions of the Gaussian quadrature rule are reasonably well approximating to the solutions. Our closed-form solutions and those of the Gaussian quadrature rule are listed in Table 8. As shown in Table 8, excellent agreements are obtained again and differences occur only at the 11-th significant digit. The testing platform is a personal computer with an Intel core i3 CPU 2.4GHz and 4GB RAM. For 31 observation sites, our closed-form formula takes 0.0055 s and the high-order Gaussian

Table 8 Lists of the vertical gravity field computed using our analytic solution and solutions by the Gaussian quadrature rules with $512 \times 512 \times 512$ points and $5 \times 5 \times 5$ points for the prism model shown in Fig. 2a with $\lambda(\mathbf{r}) = z^4$

x (km)	Gaussian quadrature solutions (mGal) with $512 \times 512 \times 512$ points	our analytic solution (mGal)	Gaussian quadrature solutions (mGal) with $5 \times 5 \times 5$ points
0	7.12219101489056	7.12219101489085	7.1221888320710950993
1	8.48056770614467	8.48056770614382	8.4805617391125540649
2	10.1696894406181	10.1696894406191	10.169676418630798409
3	12.2782706524876	12.2782706524853	12.278247766243397976
4	14.9143130178865	14.9143130178878	14.914288054727569133
5	18.2021319910864	18.2021319910878	18.202160056789619347
6	22.2702667632913	22.2702667632900	22.27054518097238045
7	27.2226356973335	27.2226356973329	27.223663649822459121
8	33.0839167397600	33.0839167397592	33.086832035778186878
9	39.7152373831687	39.7152373831755	39.724588628867728346
10	46.7187463141761	46.7187463141865	46.746050499737350492
11	53.4225546453986	53.4225546453996	53.461645509154095635
12	59.1380804111197	59.1380804111283	59.215084132472277645
13	63.4175287134867	63.4175287134972	63.441261544998837962
14	66.0399955350939	66.0399955350872	66.068292518952773662
15	66.9207406119316	66.9207406119341	67.047071844908117555

The observation point is located at the top surface of the prism

method using $512 \times 512 \times 512$ quadrature points takes 171.9481 s. The low-order Gaussian quadrature solution using $5 \times 5 \times 5$ quadrature points is also shown in Table 8 which takes 0.0005540 s computation time for 31 observation sites. Although the computational speed of the low-order Gaussian quadrature rule is ten times faster than that of our analytic formula, it has 0.1–0.2% relative errors at observation sites approaching to the center of the top surface. Compared to our closed-form solution, the low-order Gaussian quadrature rule has 0.001–0.039 mGal differences for the vertical gravity field. As these differences are already larger than instrumental accuracy (0.002–0.010 mGal), solutions computed by this low-order Gaussian quadrature rule are undesired.

4 Discussion and Conclusions

In comparison with previously published work, our approaches of computing the gravitational potential and acceleration due to arbitrary polyhedral bodies have adopted a generalized singularity-free framework. This allowed to derive closed-form solutions of the gravitational potential and acceleration for the cases of constant and linear variations in mass density. We are the first to present closed-form solutions of the gravitational potential for a general polyhedral body with quadratic density contrast varying in all directions (x, y and z).

For a prismatic body with density contrasts varying in both horizontal and vertical directions, our approach can deliver closed-form solutions of the gravity potential caused

by constant, linear, quadratic and cubic density contrasts. For the gravitational acceleration of a prismatic body, we have shown that closed-form solutions exist in the case of constant and linear variations in density contrast. To our best knowledge, we deliver the first closed-form solutions of the gravitational acceleration for a prismatic body with quartic density contrast, if the density contrast only varies along the z-axis.

In summary, we find:

1. For an arbitrarily polyhedral body, analytic formulae of the gravity potential and the gravity field are available in the case of $m \leq 1$, $n \leq 1$ and $t \leq 1$. For the gravity potential, an analytic formula is also available in the case of $m = 2$, $n = 2$ and $t = 2$.
2. For a prismatic body, an analytic formula exists in the case of $m \leq 3$, $n \leq 3$ and $t \leq 3$ for the gravity potential. For the gravity field, closed-form solutions are available only in the case of $m \leq 1$, $n \leq 1$ and $t \leq 4$.

Since simulation results from closed-form solutions for complicated polyhedral and spatial variations of density contrasts were not available in the literature, a simple prismatic model with a purely depth-dependent polynomial density contrast and a polyhedral body in form of a triangular prism with constant density contrasts had to be considered to verify our new analytic formulae. Excellent agreement between the results of the published analytic formulae and our results is demonstrated, verifying the accuracies of our new analytic expressions of the gravity anomaly.

Due to its ability for dealing with cases of locating observation sites at corners, on edges or on surfaces of a polyhedral body, our new analytic formula is a useful tool to compute the gravity anomaly in the immediate vicinity of the mass source body. It should have high potential in aiding interpretation of gravity data for gravity modeling problems where high accuracy is required, such as terrain correction and borehole gravity problems or in near field computation in associated fast multipole method acceleration techniques.

An interesting aspect of the new formulae is that they allow representing a density distribution with relatively few parameters, since the density is allowed to vary within a single polyhedron. This is an interesting aspect, when it comes to inversion, because these will reduce some of the ambiguities and may require less regularization.

Acknowledgements This study was supported by Grants from the National Basic Research Program of China (973-2015CB060200), the Project of Innovation-driven Plan in Central South University (2016CX005), the National Science Fundation of China (41574120, 41474103, 41204082), the State High-Tech Development Plan of China (2014AA06A602), and an award for outstanding young scientists by Central South University (Lieying program 2013).

Appendix: Closed Forms for Edge Integrals

We begin to derive the closed forms for edge integrals B_j^{q+2} and $\mathbf{B}_j^{q+2}$. In Fig. 1, given the edge $C_j \in \partial H_i$ with two ordered vertices v_0 and v_1, the unit tangential vector of edge C_j is $\hat{\mathbf{e}}_j = (\mathbf{v}_1 - \mathbf{v}_0)/|\mathbf{v}_1 - \mathbf{v}_0|$. Edge C_j is parametrized by a single variable s, $s = (\mathbf{r} - \mathbf{o}) \cdot \hat{\mathbf{e}}_j$. Furthermore, $R = |\mathbf{r}' - \mathbf{r}| = (h_i^2 + m_j^2 + s^2)^{1/2}$, $(\mathbf{r} - \mathbf{o}) = \rho\hat{\boldsymbol{\rho}}$, and $\hat{\boldsymbol{\rho}}$ is a unit vector pointing from point $\mathbf{o}$ to point $\mathbf{r}$. The solid angle in Eqs. (33) and (34) is calculated as (Wilton et al. 1984)

$$\beta(\mathbf{o}) = \sum_{j=1}^{M} \beta(\mathbf{o})_j = \sum_{j=1}^{M} \hat{\mathbf{m}}_j \cdot \hat{\boldsymbol{\rho}}_j^{\perp} \left(\arctan \frac{s_1}{|m_j|} - \arctan \frac{s_0}{|m_j|} \right). \tag{48}$$

Here $\hat{\rho}_j^{\perp}$ is the unit vector from point $\mathbf{o}$ to point $\mathbf{r}_{\perp}$. At point $\mathbf{r}_{\perp}$, $s = 0$. When point $\mathbf{o}$ is inside the polygon ∂H_i, $\beta(\mathbf{o}) = 2\pi$; $\beta(\mathbf{o}) = \pi$ when point $\mathbf{o}$ is on an edge of polygon ∂H_i; $\beta(\mathbf{o}) = \Theta$ when point $\mathbf{o}$ is at a corner of polygon ∂H_i with the corner angle Θ; $\beta(\mathbf{o}) = 0$ when point $\mathbf{o}$ is outside of polygon ∂H_i.

Using the integral tables from Gradshteyn and Ryzhik (1994, equation (2.260.2)), we get

$$\begin{aligned}\mathbf{B}_j^{q+2} &= \hat{\mathbf{m}}_j \int_{C_j} R^{q+2} \mathrm{d}l = \hat{\mathbf{m}}_j \int_{s_0}^{s_1} \left(\sqrt{h_i^2 + m_j^2 + s^2}\right)^{q+2} \mathrm{d}s \\ &= \frac{\hat{\mathbf{m}}_j}{q+3} s R^{q+2} \,|_{s_0}^{s_1} + \hat{\mathbf{m}}_j \frac{q+2}{q+3} (h_i^2 + m_j^2) \int_{C_j} R^q \mathrm{d}l,\end{aligned} \tag{49}$$

where s_0 and s_1 are the parametrized coordinates of the vertices $\mathbf{v}_0$ and $\mathbf{v}_1$, respectively. To compute the gravity field (with $q = -1, 1$), we only need to calculate terms $\int_{C_j} R \mathrm{d}l$ and $\int_{C_j} R^3 \mathrm{d}l$ which are regular even if the observation site $\mathbf{r}'$ is located on an edge C_j. The initial value for the recursive algorithm given by Eq. (49) is

$$\int_{C_j} R \mathrm{d}l = \frac{1}{2}\{(h_i^2 + m_j^2) \ln \frac{s_1 + R_1}{s_0 + R_0} + s_1 R_1 - s_0 R_0\}, \tag{50}$$

where R_1 and R_0 are the distances from the point $\mathbf{r}'$ to the vertices $\mathbf{v}_0$ and $\mathbf{v}_1$, respectively. When the observation site $\mathbf{r}'$ is located on an edge C_j, we simply set $(h_i^2 + m_j^2) = 0$ which eliminates the possible logarithmic singularity in expression (50).

Now, we deal with term $B_j^{q+2} = \int_{C_j} \frac{R^{q+2}}{\rho^2} \mathrm{d}l$ $(q = -1, 1)$ in Eq. (34). When $q = -1$, we have,

$$\begin{aligned}B_j^1 = m_j \int_{C_j} \frac{R}{\rho^2} \mathrm{d}l &= m_j \int_{s_0}^{s_1} \frac{\sqrt{h_i^2 + m_j^2 + s^2}}{m_j^2 + s^2} \mathrm{d}s \\ &= m_j \left(\frac{|h_i| \arctan(\frac{|h_i| s}{m_j R})}{m_j} + \ln(s + R) \right) |_{s_0}^{s_1} \\ &= |h_i| \left(\arctan \frac{|h_i| s_1}{m_j R_1} - \arctan \frac{|h_i| s_0}{m_j R_0} \right) + m_j \ln \frac{s_1 + R_1}{s_0 + R_0}.\end{aligned} \tag{51}$$

When $q = 1$, we have,

$$\begin{aligned}B_j^3 = m_j \int_{C_j} \frac{R^3}{\rho^2} \mathrm{d}l &= m_j \int_{s_0}^{s_1} \frac{(\sqrt{h_i^2 + m_j^2 + s^2})^3}{m_j^2 + s^2} \mathrm{d}s \\ &= m_j \left[\frac{|h_i|^3 \arctan(\frac{|h_i| s}{m_j R})}{m_j} + \frac{1}{2}(3h_i^2 + m_j^2) \ln(s + R) + \frac{1}{2} s R \right] |_{s_0}^{s_1} \\ &= |h_i|^3 \left(\arctan \frac{|h_i| s_1}{m_j R_1} - \arctan \frac{|h_i| s_0}{m_j R_0} \right) \\ &\quad + \frac{1}{2} m_j (3h_i^2 + m_j^2) \ln \frac{s_1 + R_1}{s_0 + R_0} + \frac{1}{2} m_j (s_1 R_1 - s_0 R_0)\end{aligned} \tag{52}$$

In the above two equations, $m_j = (\mathbf{r} - \mathbf{o}) \cdot \hat{\mathbf{m}}_j$ for $\mathbf{r} \in C_j$, therefore m_j can take both

positive and negative values. When the observation site $\mathbf{r}'$ is located on an edge C_j of the plane ∂H_i, that is, $m_j = 0$ and $h_i = 0$, the above two integrals are free of singularities as we simply have $B_j^1 = 0$ and $B_j^3 = 0$. In Eq. (52), as $\frac{\arctan 1/m_j}{m_j}$ is an even function with respect to m_j, the sign of m_j does not affect the value of the function.

References

Abtahi SM, Pedersen LB, Kamm J, Kalscheuer T (2016) Consistency investigation, vertical gravity estimation and inversion of airborne gravity gradient tensor data—a case study from northern Sweden. Geophysics 81(3):B65–B76

Bajracharya S, Sideris M (2004) The Rudzki inversion gravimetric reduction scheme in geoid determination. J Geod 78(4–5):272–282. doi:10.1007/s00190-004-0397-y

Banerjee B, Das Gupta SP (1977) Gravitational attraction of a rectangular parallelepiped. Geophysics 42(5):1053–1055. doi:10.1190/1.1440766

Barnett CT (1976) Theoretical modeling of the magnetic and gravitational fields of an arbitrarily shaped three-dimensional body. Geophysics 41(6):1353–1364. doi:10.1190/1.1440685

Beiki M, Pedersen LB (2010) Eigenvector analysis of gravity gradient tensor to locate geologic bodies. Geophysics 75(6):I37–I49. doi:10.1190/1.3484098

Blakely RJ (1996) Potential theory in gravity and magnetic applications. Cambridge University Press, Cambridge

Cai Y, Cy Wang (2005) Fast finite-element calculation of gravity anomaly in complex geological regions. Geophys J Int 162(3):696–708. doi:10.1111/j.1365-246X.2005.02711.x

Chai Y, Hinze WJ (1988) Gravity inversion of an interface above which the density contrast varies exponentially with depth. Geophysics 53(6):837–845. doi:10.1190/1.1442518

Conway J (2015) Analytical solution from vector potentials for the gravitational field of a general polyhedron. Celest Mech Dyn Astron 121(1):17–38. doi:10.1007/s10569-014-9588-x

Conway JT (2016) Vector potentials for the gravitational interaction of extended bodies and laminas with analytical solutions for two disks. Celest Mech Dyn Astron 125(2):161–194. doi:10.1007/s10569-016-9679-y

De Castro DL, Fuck RA, Phillips JD, Vidotti RM, Bezerra FH, Dantas EL (2014) Crustal structure beneath the Paleozoic Parnaíba Basin revealed by airborne gravity and magnetic data, Brazil. Tectonophysics 614:128–145

D'Urso MG (2013) On the evaluation of the gravity effects of polyhedral bodies and a consistent treatment of related singularities. J Geod 87(3):239–252. doi:10.1007/s00190-012-0592-1

D'Urso MG (2014a) Analytical computation of gravity effects for polyhedral bodies. J Geod 88(1):13–29. doi:10.1007/s00190-013-0664-x

D'Urso MG (2014b) Gravity effects of polyhedral bodies with linearly varying density. Celest Mech Dyn Astron 120(4):349–372. doi:10.1007/s10569-014-9578-z

D'Urso MG (2015) The gravity anomaly of a 2D polygonal body having density contrast given by polynomial functions. Surv Geophys 36(3):391–425. doi:10.1007/s10712-015-9317-3

D'Urso MG (2016) A remark on the computation of the gravitational potential of masses with linearly varying density. Springer, Cham, pp 205–212. doi:10.1007/1345_2015_138

Farquharson C, Mosher C (2009) Three-dimensional modelling of gravity data using finite differences. J Appl Geophys 68(3):417–422

García-Abdeslem J (1992) Gravitational attraction of a rectangular prism with depth-dependent density. Geophysics 57(3):470–473. doi:10.1190/1.1443261

García-Abdeslem J (2005) The gravitational attraction of a right rectangular prism with density varying with depth following a cubic polynomial. Geophysics 70(6):J39–J42. doi:10.1190/1.2122413

Gradshteyn I, Ryzhik IM (1994) Table of integrals, series and products. Academic Press, New York

Grant FS, West GF (1965) Interpretation theory in applied geophysics, vol 130. McGraw-Hill, New York

Hamayun IP, Tenzer R (2009) The optimum expression for the gravitational potential of polyhedral bodies having a linearly varying density distribution. J Geod 83:1163–1170

Hansen RO (1999) An analytical expression for the gravity field of a polyhedral body with linearly varying density. Geophysics 64(1):75–77. doi:10.1190/1.1444532

Holstein H (2002) Gravimagnetic similarity in anomaly formulas for uniform polyhedra. Geophysics 67(4):1126–1133. doi:10.1190/1.1500373

Holstein H (2003) Gravimagnetic anomaly formulas for polyhedra of spatially linear media. Geophysics 68(1):157–167. doi:10.1190/1.1543203
Holstein H, Ketteridge B (1996) Gravimetric analysis of uniform polyhedra. Geophysics 61(2):357–364. doi:10.1190/1.1443964
Jahandari H, Farquharson CG (2013) Forward modeling of gravity data using finite-volume and finite-element methods on unstructured grids. Geophysics 78(3):G69–G80
Jin J (2002) The finite element method in electromagnetics. Wiley-IEEE Press, New York
Kaftan I, Salk M, Sari C (2005) Application of the finite element method to gravity data case study: western Turkey. J Geodyn 39(5):431–443
Kamm J, Lundin IA, Bastani M, Sadeghi M, Pedersen LB (2015) Joint inversion of gravity, magnetic, and petrophysical data—a case study from a gabbro intrusion in Boden, Sweden. Geophysics 80(5):B131–B152. doi:10.1190/geo2014-0122.1
Kwok YK (1991) Gravity gradient tensors due to a polyhedron with polygonal facets. Geophys Prospect 39(3):435–443. doi:10.1111/j.1365-2478.1991.tb00320.x
Lelièvre PG, Farquharson CG, Hurich CA (2012) Joint inversion of seismic traveltimes and gravity data on unstructured grids with application to mineral exploration. Geophysics 77(1):K1–K15. doi:10.1190/geo2011-0154.1
Li Y, Oldenburg DW (1998) 3-D inversion of gravity data. Geophysics 63(1):109–119. doi:10.1190/1.1444302
Martín-Atienza B, García-Abdeslem J (1999) 2-D gravity modeling with analytically defined geometry and quadratic polynomial density functions. Geophysics 64(6):1730–1734. doi:10.1190/1.1444677
Martinez C, Li Y, Krahenbuhl R, Braga MA (2013) 3D inversion of airborne gravity gradiometry data in mineral exploration: a case study in the Quadrilátero Ferrífero, Brazil. Geophysics 78(1):B1–B11. doi:10.1190/geo2012-0106.1
Moorkamp M, Heincke B, Jegen M, Roberts AW, Hobbs RW (2011) A framework for 3-D joint inversion of MT, gravity and seismic refraction data. Geophys J Int 184(1):477–493
Nagy D (1966) The gravitational attraction of a right rectangular prism. Geophysics 31(2):362–371. doi:10.1190/1.1439779
Nagy D, Papp G, Benedek J (2000) The gravitational potential and its derivatives for the prism. J Geod 74(7–8):552–560. doi:10.1007/s001900000116
Okabe M (1979) Analytical expressions for gravity anomalies due to homogeneous polyhedral bodies and translations into magnetic anomalies. Geophysics 44(4):730–741. doi:10.1190/1.1440973
Paul MK (1974) The gravity effect of a homogeneous polyhedron for three-dimensional interpretation. Pure Appl Geophys 112(3):553–561. doi:10.1007/BF00877292
Petrović S (1996) Determination of the potential of homogeneous polyhedral bodies using line integrals. J Geod 71(1):44–52. doi:10.1007/s001900050074
Pohanka V (1988) Optimum expression for computation of the gravity field of a homogeneous polyhedral body. Geophys Prospect 36(7):733–751. doi:10.1111/j.1365-2478.1988.tb02190.x
Pohanka V (1998) Optimum expression for computation of the gravity field of a polyhedral body with linearly increasing density. Geophys Prospect 46(4):391–404. doi:10.1046/j.1365-2478.1998.960335.x
Rao DB (1990) Analysis of gravity anomalies of sedimentary basins by an asymmetrical trapezoidal model with quadratic density function. Geophysics 55(2):226–231. doi:10.1190/1.1442830
Roberts AW, Hobbs RW, Goldstein M, Moorkamp M, Jegen M, Heincke B (2016) Joint stochastic constraint of a large data set from a salt dome. Geophysics 81(2):ID1–ID24
Smith DA (2000) The gravitational attraction of any polygonally shaped vertical prism with inclined top and bottom faces. J Geod 74(5):414–420. doi:10.1007/s001900000102
Tsoulis D, Wziontek H, Petrovic S (2003) A bilinear approximation of the surface relief in terrain correction computations. J Geod 77(5–6):338–344. doi:10.1007/s00190-003-0332-7
Tsoulis D (2012) Analytical computation of the full gravity tensor of a homogeneous arbitrarily shaped polyhedral source using line integrals. Geophysics 77(2):F1–F11. doi:10.1190/geo2010-0334.1
Tsoulis D, Petrović S (2001) On the singularities of the gravity field of a homogeneous polyhedral body. Geophysics 66(2):535–539. doi:10.1190/1.1444944
Van der Meijde M, Juli J, Assumpo M (2013) Gravity derived Moho for South America. Tectonophysics 609:456–467
Waldvogel J (1979) The Newtonian potential of homogeneous polyhedra. Zeitschrift für angewandte Mathematik und Physik ZAMP 30(2):388–398. doi:10.1007/BF01601950
Werner RA (1994) The gravitational potential of a homogeneous polyhedron or don't cut corners. Celest Mech Dyn Astron 59(3):253–278. doi:10.1007/BF00692875

Wilton D, Rao S, Glisson A, Schaubert D, Albundak O, Butler C (1984) Potential integrals for uniform and linear source distributions on polygonal and polyhedral domains. IEEE Trans Antennas Propag 32(3):276–281

Zhang HL, Ravat D, Marangoni YR, Hu XY (2014) NAV-Edge: edge detection of potential-field sources using normalized anisotropy variance. Geophysics 79(3):J43–J53. doi:10.1190/geo2013-0218.1

Zhou X (2009a) 3D vector gravity potential and line integrals for the gravity anomaly of a rectangular prism with 3D variable density contrast. Geophysics 74(6):I43–I53. doi:10.1190/1.3239518

Zhou X (2009b) General line integrals for gravity anomalies of irregular 2D masses with horizontally and vertically dependent density contrast. Geophysics 74(2):I1–I7. doi:10.1190/1.3073761